Computers in Biology and Medicine 184 (2025) 109420

Contents lists available at ScienceDirect

Computers in Biology and Medicine

journal homepage: www.elsevier.com/locate/compbiomed

Hybrid physics-based and data-driven modeling of vascular bifurcation pressure differences

Natalia L. Rubio, Luca Pegolotti, Martin R. Pfaller, Eric F. Darve, Alison L. Marsden *

Stanford University, United States of America

ARTICLE INFO

Keywords:
Cardiovascular fluid mechanics
Reduced-order modeling
Data-driven modeling
Machine learning
Pressure loss models

ABSTRACT

Reduced-order models allow for the simulation of blood flow in patient-specific vasculatures. They offer a significant reduction in computational cost and wait time compared to traditional computational fluid dynamics models. Unfortunately, due to the simplifications made in their formulations, reduced-order models can suffer from significantly reduced accuracy. One common simplifying assumption is that of continuity of static or total pressure over vascular bifurcations. In many cases, this assumption has been shown to introduce significant errors in pressure predictions. We propose a model to account for this pressure difference, with the ultimate goal of increasing the accuracy of cardiovascular reduced-order models. Our model successfully uses a structure common in existing reduced-order models in conjunction with machine-learning techniques to predict the pressure difference over a vascular bifurcation. We analyze the performance of our model on steady and transient flows, testing it on three bifurcation cohorts representing three different bifurcation geometric types. We find that our model makes significantly more accurate predictions than other models for approximating bifurcation pressure losses commonly used in the reduced-order cardiovascular modeling community. We also compare the efficacy of different machine-learning techniques and observe that a neural network performs most robustly. Additionally, we consider two different model modalities: one in which the model is fit using both steady and transient flows, and one in which it is optimized for performance in transient flows. We discuss the trade-off between the physical interpretability associated with the first option and the improved accuracy in transient flows associated with the latter option. We also demonstrate the model's ability to generalize by testing it on a combined dataset containing two different bifurcation types. This work marks a step towards improving the accuracy of cardiovascular reduced-order models, thereby increasing their utility for cardiovascular flow modeling.

1. Introduction

In the last 20 years, computational fluid dynamics (CFD) simulations of cardiovascular flows have been established as a valuable tool in clinical decision making, understanding mechanisms of cardiovascular disease progression, and the design of medical devices [1–5]. First, they shed insight into clinical decision making for cardiovascular disease. Cardiovascular flow simulations are used to analyze flows in patient-specific vasculatures and the associated health outcomes. For instance, in [6–9], CFD models were used to analyze flow through coronary artery aneurysms of patients with Kawasaki disease, and the analysis yielded metrics that correlated with thrombotic risk. CFD simulations are also used to inform surgical planning. They provide patient-specific insights into the characteristics of a diseased anatomy that allow clinicians to customize the patient's treatment, rather than using a "one-size-fits-all" approach. Furthermore, CFD models predict the changes in flow behavior that would result from hypothetical surgical modifications. For instance, in the context of multi-stage surgical intervention for single-ventricle heart defects, CFD flow analysis was used to compare two candidate stage 2 operations, the hemi-Fontan and bidirectional Glenn procedures, study patient-specific effects of the hemi-Fontan procedure under varying physiological states, and analyze the effects of geometric variations in anatomies constructed by the stage 3 Fontan procedure [10–12]. Second, cardiovascular flow simulations have contributed to our understanding of cardiovascular biomechanics and mechanobiology by characterizing hemodynamics that are difficult to observe experimentally. For example, CFD simulations made instrumental contributions to our understanding of the mechanisms driving the development of pulmonary arterial hypertension by modeling flows in smaller, distal vessels that are difficult to characterize experimentally [13–16]. Third, cardiovascular flow simulations allow for design testing in a low-cost, low-risk setting, which is invaluable in

* Corresponding author.
E-mail addresses: nrubio@stanford.edu (N.L. Rubio), amarsden@stanford.edu (A.L. Marsden).

https://doi.org/10.1016/j.compbiomed.2024.109420
Received 23 February 2024; Received in revised form 24 October 2024; Accepted 8 November 2024
Available online 28 November 2024

the engineering and optimization of cardiovascular medical devices and treatments including stents [17–19], grafts [20–23], circulatory support systems [24–27], and vascular drug delivery systems [28–30].

Traditional CFD models solve the unsteady Navier–Stokes equations in three dimensions (3D), a computationally intensive task. While these simulations have demonstrated clear clinical, scientific, and engineering value, their computational cost is a barrier to widespread adoption in clinical settings (especially emergency scenarios), real-time analysis, and multi-query applications. Reduced-order models (ROMs) are simplified representations of cardiovascular flows that predict bulk properties at much lower computational cost, providing a computationally tractable alternative to 3D simulations. ROMs have been used to find boundary and initial conditions for higher-fidelity simulations [31–36], for uncertainty quantification [37–39], and as stand-alone models [40–42]. Zero-dimensional (0D) and one-dimensional (1D) ROMs are two of the most frequently used in the cardiovascular flow modeling community [43–47].

In the 0D ROM formulation, a vasculature is represented by an idealized electric circuit in which flow and pressure are analogous to current and voltage, respectively. Vessels are represented by wires containing circuit elements (e.g., resistors, capacitors, and inductors) with characteristic values capturing the 3D vessel geometry. The bulk flow and pressure values at the inlets and outlets of each branch in the vasculature are given by the values of current and pressure at the corresponding nodes in the analogous electric circuit [33,48–50]. In the 1D ROM, the flow through the vasculature is modeled using a one-dimensional partial differential equation (PDE) enforcing conservation of mass and momentum, derived by integrating across the vessel cross-section [43,51–56].

While ROMs are promising tools for high-speed, computationally lightweight modeling of cardiovascular flows, they suffer from reduced accuracy due to the simplifications in their formulations. One such simplification occurs in the handling of bifurcations. Bifurcations generally feature flow separation and other nonlinear behaviors that cannot be modeled with the ROMs described above. Frequently, continuity of either static [36,44,57–59] or total [60–65] pressure is assumed over a bifurcation. Practical experience and high-fidelity CFD simulations, however, indicate that significant differences in both static and total pressure between the inlets and outlets of a bifurcation can exist. Indeed, previous work has shown that the treatment of bifurcations has a notable effect on ROM solutions [48,66–71]. As such, there is a need to develop and incorporate models that accurately predict pressure differences over vascular bifurcations to improve ROM accuracy. Past studies have proposed such models specifically for cardiovascular flows and other flow networks featuring bifurcations [72–74]. These models vary in complexity and are generally developed using a combination of physics-based and empirical approaches.

In recent years, however, as computational blood flow models have gained traction, more 3D cardiovascular CFD data has become available [75]. In parallel, significant advances have been made in data-driven modeling techniques. Given these developments, we present a novel, hybrid approach for modeling pressure differences over bifurcations in ROMs. Specifically, we propose accounting for pressure differences by augmenting bifurcation outlet branches with a 0D bifurcation element comprising a serially connected resistor, quadratic resistor, and inductor whose characteristic values are determined from the bifurcation geometry using machine learning (ML) techniques. In doing so, we apply ML techniques to our problem within a constrained, physics-based framework that reduces the complexity of the regression problem and provides interpretability.

In Section 2, Methods, we discuss the structure of our model and how it is intended to integrate into existing ROM schemata. Next, we describe the procedure used to generate training data for the machine learning components of our model. In Section 3, Results, we show that our hybrid physics-based data-driven model structure can accurately predict the pressure difference over bifurcations with previously unseen geometries for three different cohorts of geometries in both steady and transient flow settings. We also consider several ML regression techniques and compare their effectiveness for our task. We identify the major takeaways of this study and relate them to the broader field of cardiovascular ROMs in Section 4, Discussion. Finally, in Section 5, Limitations and Future Work, we discuss the contributions of our model towards reduced-order cardiovascular modeling, summarize its current limitations, and propose future work to develop the model further and deploy it in existing ROMs.

2. Methods

In most ROM solvers, and in this work, pressure drops are computed between the inlet and each outlet individually. We indicate the bifurcation inlet with the subscript *"inlet"*, the outlet over which we are currently computing the pressure difference with the subscript *"outlet,1"*, and the second outlet of the bifurcation, over which we are not currently computing the pressure difference, with the subscript *"outlet,2"*. In most ROMs, a pressure difference over a vascular junction is prescribed by the inclusion of an equation relating the pressure at the inlet branch to the pressure, P at each outlet branch. In the context of Fig. 1, this corresponds to setting the quantity $P_{\text{outlet},1} - P_{\text{inlet}}$, which we hereafter refer to as ΔP, to some value. It is common to enforce conservation of static pressure so that

$$\Delta P_{\text{static pressure}} = 0. \tag{1}$$

Similarly, the equation

$$\Delta P_{\text{total pressure}} = \frac{1}{2}\rho(u^2_{\text{inlet}} - u^2_{\text{outlet},1}), \tag{2}$$

where ρ is the density of blood, enforces continuity of total pressure.

Aside from continuity of total and static pressure, the most commonly used model for pressure differences over vascular bifurcations is the Unified0D+ model, proposed in 2015 [68,74,76–78]. It predicts the pressure difference over bifurcations as follows,

$$\Delta P_{\text{Unified0D+}} = \left(1 - \frac{u_{\text{inlet}}}{u_{\text{outlet},1}} \cos\left[\frac{3}{4}(\pi - \theta)\right]\right) \rho u^2_{\text{outlet},1}, \tag{3}$$

where u_{outlet} is the outlet velocity, u_{inlet} is the velocity in the inlet branch, and θ is the angle between the outlet and inlet branch. The Unified0D+ model incorporates physical principles such as conservation of mass, momentum, and energy along with empirically fitted corrections, but the absence of a term involving the time derivative of the flow limits the Unified0D+ model's ability to make accurate predictions on transient flow. A major contribution of [74] was the introduction of a pseudodatum branch. The pseudodatum is a modified inlet whose properties capture the effective behavior of multiple inlets and account for energy exchange between branches. Although not needed for the bifurcations considered in this work, the ability to accommodate junctions with arbitrary numbers of inlets and outlets is a major advantage of the Unified0D+ model. In Section 5, we discuss a potential extension to our proposed model to handle these more complex junction types.

The Unified0D+ model predicts the pressure drop at the point at which the centerline bifurcates. In contrast, our model predicts the pressure loss between the inlet and outlet of a bifurcation, some distance upstream and downstream of the bifurcation point. We are interested in ΔP between the inlet and outlet as it encompasses the effects of the entire junction region, and it is the quantity needed in most ROM solvers. To compare the Unified 0D+ model to ours, we therefore add the pressure differences expected in the vessel segment between the inlet and bifurcation point and between the bifurcation point and outlet to the pressure difference predicted by the Unified0D+ model. The pressure differences in the inlet and outlet vessels are calculated assuming Poiseuille resistance as follows

$$\Delta P = \Delta P_{\text{Unified0D+}} + \Delta P_{\text{Poiseuille adjustment}} - \frac{8\mu L_{\text{inlet}} Q_{\text{inlet}}}{\pi r^4_{\text{inlet}}}$$

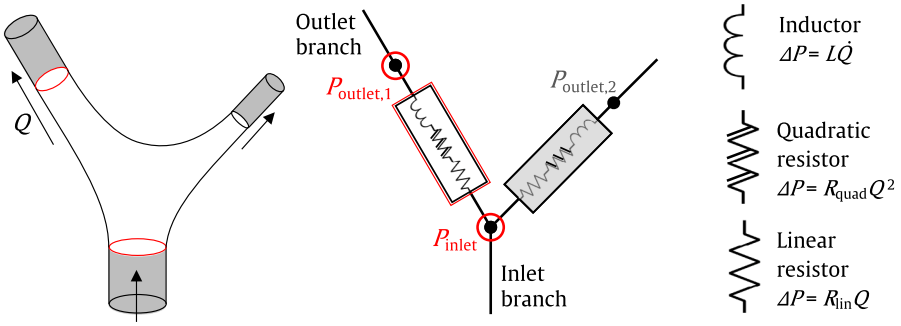

Fig. 1. 3D vascular bifurcation (left) and its representation in a ROM (center) including the proposed RRI bifurcation block, featuring a linear resistor, quadratic resistor, and inductor (right).

$$-\frac{8\mu L_{outlet}Q_{outlet}}{\pi r_{outlet}^4}, \tag{4}$$

where μ is the viscosity of blood and L is the length of the vessel. $\Delta P_{\text{Poiseuille adjustment}}$ is a correction given in [74] to be used when combining the Unified0D+ model with the Poiseuille equation-based vessel pressure difference model in this manner. This system is similar to the approach taken in [79].

2.1. Resistor–resistor–inductor model

We propose to model the pressure difference between the inlet and outlet of a bifurcation as a linear combination of the outlet flow, Q, the square of the outlet flow Q^2, and the time derivative of the flow $\dot{Q}$ as follows

$$\Delta P_{RRI} = R_{lin}(\mathcal{G})Q + R_{quad}(\mathcal{G})Q^2 + L(\mathcal{G})\dot{Q}. \tag{5}$$

In the context of the circuit analogy, this formulation is equivalent to inserting a 0D block consisting of a serially connected resistor with resistance R_{lin}, quadratic resistor with resistance R_{quad}, and inductor with inductance L between the inlet and each outlet of a bifurcation. For this reason, we hereafter refer to it as the Resistor–Resistor–Inductor (RRI) model. As discussed above, this model structure is well-established in the cardiovascular ROM community for modeling blood vessels [48,50]. In blood vessel modeling, the characteristic values, R_{quad}, R_{lin}, and L, can be determined from the vessel geometry using formulas based on simplifications of the Navier–Stokes equations. However, due to the more complex and irregular nature of bifurcating flows, no such formulas are readily apparent for bifurcation geometries [50,80]. A key contribution of this work is the use of data-driven methods to predict the characteristic values in the absence of physics-based relations.

In the RRI model, the linear resistor captures pressure losses proportional to the flow rate—generally associated with viscous energy losses in steady, laminar flow. The quadratic resistor captures energy losses associated with flow separation and nonlinear effects, which are generally observed at the expansion of the bifurcation. Quadratic resistors are similarly used to represent stenosed vessels, which feature similar separation at the expansion [49,81,82]. Lastly, the inductor describes pressure differences proportional to the change in flow over time, induced by changes in the flow's inertia. In steady analyses, we refer to the Resistor–Resistor (RR) model where there is no inductance ($L = 0$). The RRI formulation assumes no wall compliance, although the model may be extended to account for wall compliance by the inclusion of a capacitor. Preliminary studies showed that the flow-pressure difference profile over a wide range of junctions resembled those shown in Figs. 6 and 7 and that the RRI model form closely replicated the relationship between the flow and pressure difference over a wide range of bifurcation geometries in both steady and transient flows (as is shown in these figures).

We determined the coefficients, R_{quad}, R_{lin}, and L, from the bifurcation's geometry $\mathcal{G}$ using data-driven models. The geometric features include $\mathcal{G}_1 = [r_{inlet}, r_{outlet,1}, r_{outlet,2}, \theta_1, \theta_2, l_1, l_2]$. These are shown in Fig. 2 and refer to the inlet radius, outlet radius, auxiliary outlet radius, outlet angle, auxiliary outlet angle, outlet length, and auxiliary outlet length, respectively. The auxiliary outlet is the bifurcation outlet for which we are not computing the pressure difference and is indicated with the subscript *"2"*.

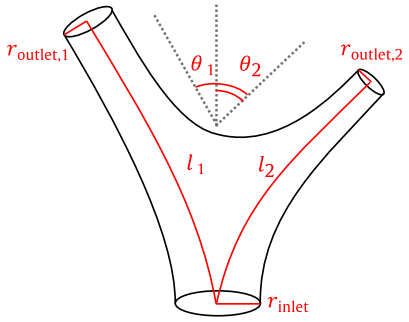

Fig. 2. Geometric parameters characterizing bifurcations and used to predict the coefficients R_{quad}, R_{lin}, and L which in turn govern the relationship between Q, Q^2, and $\dot{Q}$ and ΔP in the RRI model.

To train and validate the machine learning models, we generated synthetic bifurcation geometries and ran simulations for a series of flow conditions in each geometry to find the ground truth values of R_{quad}, R_{lin}, and L associated with that geometry.

2.2. Data generation

We generated three cohorts of idealized synthetic bifurcations representing: an isoradial cohort, a pulmonary cohort, and a brachiocephalic cohort. The isoradial cohort is representative of bifurcations analyzed in the work that led to the Unified0D+ model (although it should be noted that this study considered a wide range of outlet radii and offset angles) [74]. The pulmonary cohort is representative of distal bifurcations in the pulmonary tree. The brachiocephalic cohort is representative of the bifurcation of the brachiocephalic trunk into the right subclavian artery and the right common carotid artery. These anatomies are shown in Fig. 4. We consider the pulmonary and brachiocephalic cohorts to be the main benchmarks for our model, as they are based on bifurcations observed in the native vasculature. Both the pulmonary and brachiocephalic cohorts represent anatomies for which junction pressure modeling is crucial—the brachiocephalic bifurcation can exhibit large magnitude pressure differences, and in pulmonary anatomies, many bifurcations are often chained together, so neglecting bifurcation pressure differences can result in significant cumulative error.

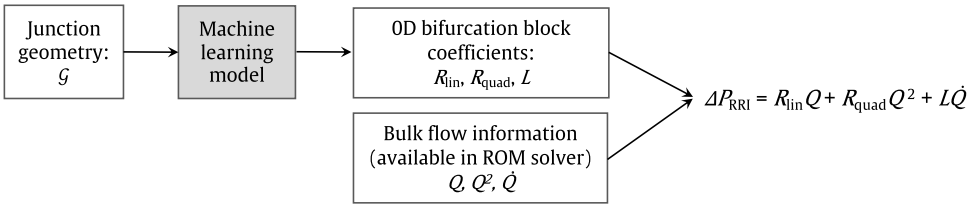

Fig. 3. Overview of the computation of a pressure difference over a vascular junction using the RRI model.

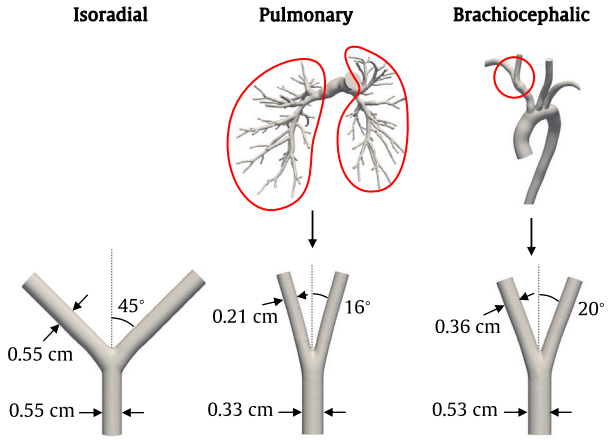

Fig. 4. Examples of pulmonary and brachiocephalic bifurcations in their surrounding vasculatures (top) and nominal idealized bifurcations from the isoradial, pulmonary, and brachiocephalic cohorts (bottom).

2.2.1. Geometry generation

The parameters defining the automated generation of the bifurcation geometries were the inlet radius, the inlet and outlet radii, and the offset angles between the inlets and outlets. For bifurcations in the isoradial bifurcation cohort, these values were chosen randomly from a uniform distribution varying ±20% of the parameter value for a nominal isoradial bifurcation. The characteristic geometric parameter values for bifurcations in the pulmonary and brachiocephalic cohorts were chosen randomly from uniform distributions spanning the 40th to 60th percentile of the range of parameter values observed in distal pulmonary and brachiocephalic bifurcations found in a publicly available database of patient-specific cardiovascular flow models, the Vascular Model Repository (VMR) [75].[1] The ranges for the characteristic bifurcation dimensions can be found in Appendix B, and their average values are reported in Fig. 4. These distributions were chosen as a proof of concept demonstrating the effectiveness of the RRI model. While we hypothesize that the RRI model would achieve similar results on wider distributions, we predict that this would require more training data, as discussed in Sections 4 and 5. This is illustrated by a supplementary study we conducted using a combined dataset made up of the brachiocephalic and pulmonary bifurcations (Section 3.3).

We used SimVascular, an open-source software suite for cardiovascular modeling and simulation [83],[2] to create a set of idealized bifurcation solid models and simulate the flow fields associated with different boundary conditions. In particular, we used the SimVascular Python API[3] to generate the geometries with automated scripts as follows. First, we specified a series of points that define the centerlines of the vessels and identify the vessel lumen at each point. Then, we lofted the vessels into solid models and merged them to form a single geometry using Boolean operations. A tetrahedral mesh was then generated from each geometry. The mesh size was chosen to be the largest at which an accurate solution was attained, as determined by the mesh convergence studies shown in Appendix A. The mesh was refined in the boundary layer as well as in a sphere surrounding the center of the junction to better resolve the complex flow behaviors in those locations.

2.2.2. Simulation

Flows through the bifurcations were simulated using the stabilized finite element solver svSolver, provided with SimVascular, to solve the three-dimensional Navier Stokes equations. A parabolic velocity profile with varying magnitude was prescribed at the inlet. The inlet velocities for the isoradial cohort were sampled from a uniform distribution varying ±20% of a nominal inlet velocity considered in [74] while the inlet velocities applied to the pulmonary and brachiocephalic cohort were sampled from a uniform distribution ranging from 40th to 60th percentile of the inlet velocity values seen in pulmonary and brachiocephalic bifurcations in the VMR. The inlet velocity ranges for each cohort are listed in Appendix B. Resistance boundary conditions were applied at the outlets with a fixed resistance value of 100 cm^2 sg^{-1} and distal pressure of 0 mmHg [50].

After the simulations were completed, we reduced the flow and pressure results to a 1D format by projection onto the model centerline. To achieve this, at each point along the centerline we integrated the velocity field from the 3D flow results over the surface defined by the intersection of the 3D vessel with a plane normal to the centerline tangent vector and containing the centerline point. Similarly, the pressure results were computed by calculating the average of the pressure field over the cross-section of the vessel normal to the centerline tangent. The flow at the outlets and change in pressure with respect to the inlet were extracted from the 1D representation. We defined inlet and outlet point locations to be about 4 inlet diameters upstream and 10 inlet diameters downstream of the bifurcation point, respectively. This distance was heuristically chosen, based on analysis of 3D flow in a range of bifurcations and flow conditions, to be large enough that we could assume the flow to be free of entrance effects and behave as fully-developed flow. In this way, we ensured that all effects of the flow behaviors caused by the bifurcation will be analyzed and accounted for in our model.

2.2.3. Characteristic value extraction

For each geometry, two types of simulations were run—steady and transient. First, two steady simulations were run at 50% and 100% of the sampled inlet flow rate. A simulation was considered to have reached a steady state when the difference between the quantities of interest (outlet flow and pressure change) at the last time step and 100 time steps before the last time step was less than 1% with a time step size of 0.001 s. Second, a transient flow simulation was run in which the flow at the inlet was varied in time following the sinusoidal profile shown in Fig. 5, where the maximum inlet flow rate was the sampled flow rate. From the simulation data, we found the coefficients R_{lin}, R_{quad}, and L for each bifurcation geometry inlet–outlet pair.

[1] http://www.vascularmodel.com (2022).
[2] https://simvascular.github.io/ (May 2023).
[3] https://simvascular.github.io/documentation/python_interface.html(May 2023).

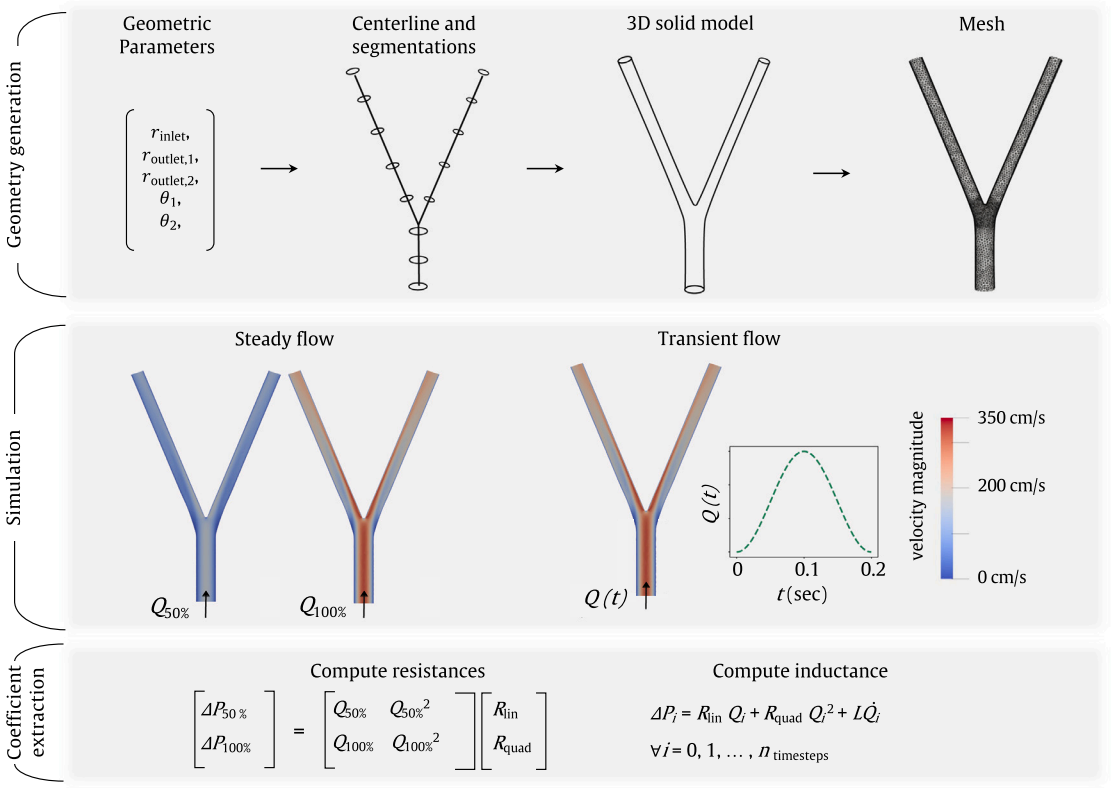

Fig. 5. Overview of data generation pipeline. First, we generated a bifurcation geometry based on a set of geometric features. Then, two steady simulations were run from which the coefficients R_{lin} and R_{quad} were determined by solving a simple system of equations containing the steady simulation results. Finally, a transient simulation was run from which the coefficient L was determined using least squares. In the TO method, all three coefficients, R_{lin}, R_{quad}, and L were determined from the transient simulation.

First, we fit the coefficients R_{lin} and R_{quad} to the results of the steady simulations by solving the system of equations

$$\begin{bmatrix} \Delta P_{50\%} \\ \Delta P_{100\%} \end{bmatrix} = \begin{bmatrix} Q_{50\%} & Q_{50\%}^2 \\ Q_{100\%} & Q_{100\%}^2 \end{bmatrix} \begin{bmatrix} R_{lin} \\ R_{quad} \end{bmatrix}, \tag{6}$$

where the subscripts 50% and 100% refer to the steady simulations run at 50% and 100% of the peak inlet flow, respectively. We also experimented with running four steady simulations (adding $Q_{25\%}$ and $Q_{75\%}$) and fitting R_{lin} and R_{quad} using least squares. We found that this did not result in significantly different values for R_{lin} and R_{quad}, so to avoid the added computational cost, we proceeded with the two-simulation fitting method described in (6).

To determine the coefficients for the transient model, we used least squares on an over-defined system of equations containing the results of the transient simulations. Each simulation timestep contributed a linear equation to the system of linear equations as follows

$$\Delta P_i = R_{lin} Q_i + R_{quad} Q_i^2 + L\dot{Q}_i \qquad \forall i = 0, 1, \ldots, n_{timesteps}. \tag{7}$$

For transient flows, we considered two methods of fitting the coefficients. In the first method, we substituted the values of R_{lin} and R_{quad} found from steady data corresponding to the same geometry into Eq. (7) and only fit L from the transient data. In the second method, we fit all three coefficients, R_{lin}, R_{quad}, and L from the transient data. We refer to the coefficients generated using the second method as transient-optimized (TO).

2.3. Machine learning models

Having built a dataset of bifurcations, we next created ML models that take the bifurcation geometry as input and output the coefficients R_{lin}, R_{quad}, and L that govern the relationship between Q, Q^2, and $\dot{Q}$ and ΔP. In particular, the ML models took as input a vector containing the geometric features of the bifurcation, $\mathcal{G}_1 = [r_{inlet}, r_{outlet,1}, r_{outlet,2}, \theta_1, \theta_2, l_1, l_2]$, and produced as output the vector containing the relevant coefficients. In the standard modality, one model trained on resistance values fit to steady data outputted R_{lin}, R_{quad}, and a second model trained transient data outputted L. In the TO method, a single ML model trained on coefficients fitted from transient data outputted all three coefficients, R_{lin}, R_{quad}, and L. For each dataset, 80% of the geometries were allocated to training the ML models and 20% to testing them. The training datasets included 149, 98, and 88 geometries, and the test sets included 38, 25, and 22 geometries for the isoradial, pulmonary, and brachiocephalic datasets, respectively.

We tested several different ML model types, including K-Nearest Neighbors (KNN), Decision Trees (DT), Linear Regression (LR), Support Vector Regression (SVR), Gaussian Process Regression (GPR), and a Neural Network (NN) [84–89]. Except for the Neural Network, each regression model was trained to minimize the squared difference between the coefficients predicted by the model and the coefficients extracted from the simulation data. The NN was trained to minimize the squared difference between the pressure difference predicted by the coefficients given by the model and the pressure drop observed from simulation data. This type of training objective was implemented only for the NN because the backpropagation method of training an NN easily accommodates a customizable loss function. Such an approach would have been much more difficult to implement for the other model types. Hyperparameter optimization for all models was conducted on the steady data from the brachiocephalic dataset using Ray Tune [90], and the optimal parameters found are reported in Appendix C.

3. Results

3.1. Steady flows

In the first phase of our study, we analyzed steady flow through bifurcations. In this case, $\dot{Q} = 0$, so there is no need to consider the inductance coefficient L. We refer to the steady, inductance-free model as the RR model. We found overall that GPR and NN had the most success predicting the steady coefficients R_{lin} and R_{quad}. The accuracies of the Unified0D+ model and our model using different regression techniques are compared in Table 1 for all three cohorts of bifurcations. In Fig. 6, we compare steady ΔP-Q profiles predicted by 3D simulation, the RR model, and the Unified0D+ model for the three bifurcation types. For each bifurcation type, we show three geometries, which differ only in the radius of the outlet vessel over which we are predicting the pressure difference. For all cohorts, we see that the ground-truth 3D simulation predicts a lower pressure at the outlet than at the inlet and that decreasing the outlet radius increases the magnitude of the pressure drop between the outlet and inlet, as expected.

We started by analyzing isoradial bifurcations similar to those considered in the original Unified 0D+ study. We observed the ΔP-Q relationships predicted by the Unified0D+ model, our approach, and the CFD simulation results. The simulated ΔP-Q relationships follow expected physical trends. In isoradial bifurcations, the total outlet area is about double that of the inlet, so flow velocity decreases in the outlets. This deceleration causes a diminished dynamic pressure in the outlets, which contributes to elevated static pressure, resulting in a larger (less negative) ΔP. This effect is heightened at higher flows, which cause more significant changes in dynamic pressure. This is illustrated in the tendency of the ΔP-Q profiles to curve upwards. The curve is more pronounced for larger outlet radii, which experience more significant changes in dynamic pressure. While our model predicts the results of the CFD simulation quite closely, the Unified0D+ model consistently under-predicts the pressure drop. The difference between the Unified0D+ model prediction and the CFD solution is more extreme at higher flow rates.

Next, we performed a similar analysis on the pulmonary and brachiocephalic cohorts. Unlike the isoradial bifurcations, these bifurcations have outlets with smaller radii than the inlet. Since the total outlet area in these bifurcations is smaller than the inlet area, the flow accelerates upon entering the outlets, contributing to a decreased static pressure at the outlets. This effect is more intense at higher flows and accounts for the concave-down shape of the ΔP-Q profiles. Predictably, we see a more dramatic downward curve in the profiles for smaller outlet radius geometries. The pulmonary bifurcations experienced flow rates similar to those of the isoradial cohort, but because the radii in the pulmonary cohort are much smaller, the pulmonary cohort exhibits higher velocities and larger pressure drops. The brachiocephalic bifurcations were exposed to even higher velocity flows than the other cohorts, and as expected, the magnitude of the pressure changes over these bifurcations is also larger. Again, our model closely matches the CFD simulation results, but the Unified0D+ model significantly underestimates the magnitude of the pressure drop.

3.2. Transient flows

Next, we tested the performance of our RRI model on transient flows, which exhibit drastically different ΔP-Q profiles from steady-state flows (Fig. 7). For the same flow rate Q, the pressure difference over the bifurcation, ΔP, can be radically different, depending on the derivative of the flow rate Q. The inductor component of our model, $L\dot{Q}$ successfully captures this effect. It is clear that without taking into account the time derivative of the flow, it is impossible to predict the pressure difference over the bifurcation with an acceptable accuracy. To illustrate this, we include the inductance-free RR model in the visualization of our results.

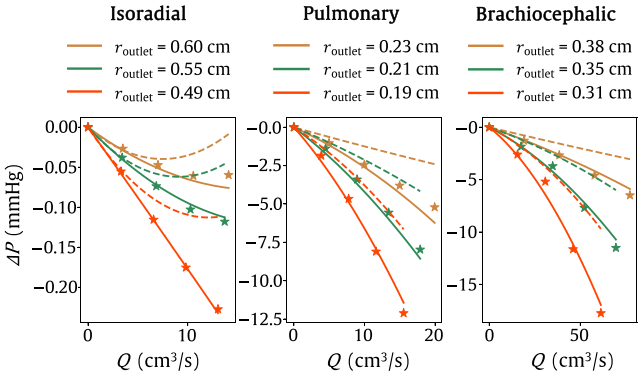

Fig. 6. Steady state ΔP vs. Q profiles for isoradial, pulmonary, and brachiocephalic type bifurcations. Solid lines show the RR model prediction, dashed lines show the Unified0D+ model prediction, and stars show simulation results. The different colors indicate different geometries, identical except for the outlet radius of one outlet vessel.

In the standard RRI model, the coefficients R_{lin} and R_{quad} are fit to match the steady simulation data, and L is fit to the transient simulation data. We also tested the transient optimized (TO) model where all three coefficients, R_{lin}, R_{quad}, and L were fit to match the transient simulation data. Notably, the TO optimized fitting method produced different coefficients from those produced by the standard fitting method. We show the root mean squared relative difference (RMSRD) for R_{lin}, R_{quad}, $R_{\text{lin}}Q_{\text{max}} + R_{\text{quad}}Q_{\text{max}}^2$ in Table 2. $R_{\text{lin}}Q_{\text{max}} + R_{\text{quad}}Q_{\text{max}}^2$ corresponds to the steady component of the ΔP predicted by the RRI model under a flow Q_{max}, the largest steady flow simulated for each bifurcation. We define RMSRD as

$$\sqrt{\frac{1}{N}\sum_{i}^{N}\left(\frac{R_{\text{steady,i}} - R_{\text{TO,i}}}{R_{\text{steady,i}}}\right)^2},$$

where N is the number of bifurcation geometries in the dataset.

As expected, the RRI TO model outperforms the standard RRI model. Again, we tested multiple regression techniques in our RRI model. In the transient case, we found that, overall, the NN best predicted the coefficients L, R_{lin}, and R_{quad} (Table 3).

3.3. Combined dataset

As a final experiment, we tested the performance of the RRI model using the neural network on a combined dataset containing both the brachiocephalic and pulmonary bifurcations, as shown in Table 4. In steady flows, the combined dataset model performed worse than both the brachiocephalic and pulmonary models by about one order of magnitude. However, in transient flows, the combined dataset model achieved accuracies comparable to those of the isolated brachiocephalic and pulmonary models. We note that although the combined dataset model achieves a lower error than the brachiocephalic-specific model in some cases, this is likely because pulmonary bifurcations, with smaller total pressure differences, and therefore smaller errors, are included in the calculation of RMSE. As such, the lower error should not suggest that the combined model predicts brachiocephalic pressure differences more accurately than the brachiocephalic-specific model.

4. Discussion

We observe excellent performance of the RRI model on both steady and transient flows. In steady flows, the proposed model outperforms the Unified0D+ model on all three bifurcation cohorts. It is not surprising that the RRI model has higher accuracy than the Unified0D+ model

Table 1
Train and test root-mean-squared error in $\Delta P(Q)$ for steady flows in isoradial, pulmonary, and brachiocephalic type bifurcations using the steady RR model with different regression techniques.

Model type:	RR						Unified0D+
ML model type:	KNN	DT	LS	SVR	GPR	NN	
Isoradial							
Train RMSE (mmHg)	0.016	0.014	0.022	0.0071	0.00074	0.0061	
Test RMSE (mmHg)	0.022	0.018	0.020	0.012	0.013	0.012	0.10
Pulmonary							
Train RMSE (mmHg)	0.63	0.47	0.93	0.95	0.018	0.41	
Test RMSE (mmHg)	0.76	0.54	0.81	0.92	0.51	0.39	1.7
Brachiocephalic							
Train RMSE (mmHg)	1.3	0.87	1.3	0.28	0.056	0.16	
Test RMSE (mmHg)	1.5	1.07	1.3	0.78	0.33	0.34	4.9

Table 2
Root mean squared relative differences in R_{quad}, R_{lin}, and $R_{quad}Q_{max}^2 + R_{lin}Q_{max}$ (the steady component of ΔP predicted by the RRI model) between coefficients fit using the standard and TO methods.

RMSRD:	R_{lin}	R_{quad}	$R_{lin}Q_{max} + R_{quad}Q_{max}^2$
Brachiocephalic	23%	47%	13%
Pulmonary	14%	55%	13%

Table 3
Train and test root-mean-squared error in $\Delta P(Q)$ for transient flows in pulmonary-type and brachiocephalic-type bifurcations using the RRI model (standard and TO methods) with different regression techniques.

ML model type:	KNN	DT	LS	SVR	GPR	NN
Standard RRI model						
Pulmonary						
RRI Train RMSE (mmHg)	2.7	3.0	3.1	2.6	2.7	2.7
RRI Test RMSE (mmHg)	2.6	2.9	2.8	2.5	3.0	2.6
Brachiocephalic						
RRI Train RMSE (mmHg)	4.0	4.3	4.5	3.8	3.8	4.0
RRI Test RMSE (mmHg)	4.3	5.3	5.2	4.5	4.5	4.6
Transient Optimized (TO) RRI model						
Pulmonary						
RRI Train RMSE (mmHg)	1.4	1.3	1.6	1.7	0.27	1.2
RRI Test RMSE (mmHg)	1.5	1.2	1.3	1.6	4.0	1.2
Brachiocephalic						
RRI Train RMSE (mmHg)	2.8	2.3	2.4	1.2	0.80	1.3
RRI Test RMSE (mmHg)	3.5	3.1	3.1	2.4	2.6	2.2

Table 4
Train and test root-mean-squared error in $\Delta P(Q)$ for transient flows in pulmonary-type and brachiocephalic-type bifurcations using the RRI model (standard and TO methods) with different regression techniques.

Combined	Steady		Transient (standard)		Transient (TO)	
dataset	Train	Test	Train	Test	Train	Test
Train RMSE (mmHg)	1.8	1.5	3.8	3.4	1.6	1.5

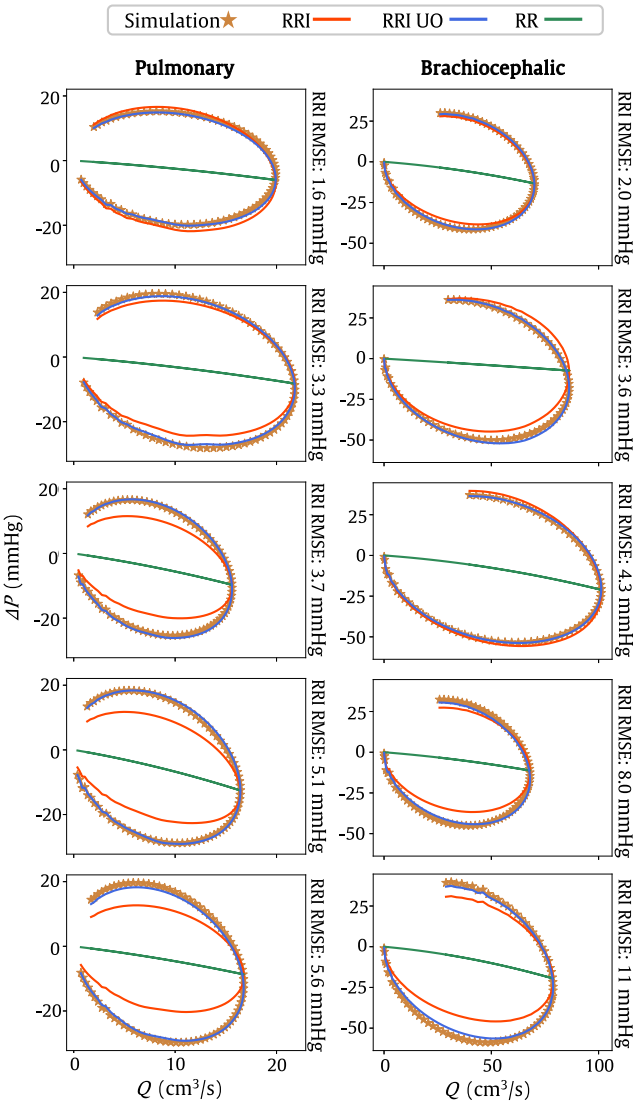

Fig. 7. Transient ΔP vs. Q profiles for test junctions from the pulmonary (left) and brachiocephalic (right) bifurcation cohorts. The sinusoidal flow profile shown in Fig. 5 was applied, where Q starts at 0, increases, and then decreases, as indicated by the arrow in the top left panel. The geometries shown are those with the lowest, 25th percentile, median, 75th percentile, and highest RMSE for the standard RRI model out of the test set, from top to bottom. We show a comparison between our RRI model (standard and TO), the inductance-free RR model, and 3D simulation results.

on pulmonary and brachiocephalic bifurcations because these bifurcations have significantly different geometric features and experience much higher velocity flows than those considered in the development of the Unified0D+ model. Furthermore, analysis of the 3D simulation results indicated that some of the assumptions used in the formulation of the Unified0D+ model, namely those about the velocity profile and distribution of total energy in the bifurcation may not be satisfied. Our model also accurately predicts pressure differences over vascular junctions in transient flows. Inductors are traditionally used to capture inertial effects in the 0D electric circuit model, so it is expected that the inclusion of an inductor in the RRI model enables improved prediction of transient behavior that is impossible to account for without considering the time derivative of the flow [50].

As expected, the TO model outperforms the standard RRI model, but the difference is slight. This indicates that bifurcation pressure differences can be cleanly split into a steady and transient component as in the standard RRI model. While marginally less accurate than the RRI TO model, the standard RRI model is more physically interpretable

because R_{lin} and R_{quad} are found solely from steady data, which is consistent with the physical definition of resistors as circuit elements containing no time-dependent physics. Furthermore, while the standard RRI model is guaranteed to recover the steady-optimized coefficients, R_{lin} and R_{quad} when $\dot{Q} = 0$, the TO model resistances were shown to differ from the steady-optimized (standard) resistances, indicating diminished adherence to the physical definition of the circuit elements. Notably, although the two different fitting methods sometimes yield quite different coefficients, they predict similar steady contributions to ΔP, allowing them both to achieve relatively good accuracy. The standard and TO model may each be preferable for different use cases, depending on the relative importance of interpretability versus accuracy. Overall, we see the highest accuracy from the NN, GPR, and SVR regression techniques. We consider the NN to be most favorable because it demonstrated consistently high accuracy, its structure integrates smoothly into a standard model framework, and it can be easily generalized to handle more complex geometries in the future (Sections 2.2, 5).

Our approach leverages physical knowledge to apply data-driven techniques in a constrained and judicious manner, providing an interpretable, robust, and practical method for predicting pressure differences over bifurcations. First, formulating the bifurcation pressure loss model as a linear resistor, quadratic resistor, and inductor is physically intuitive and consistent with commonly used cardiovascular ROM approaches. As such, it can be easily adopted by the community and implemented in existing ROM solvers. Second, our formulation takes advantage of modern machine-learning techniques but mitigates the risk of unexpected behavior generally associated with "black-box" data-driven models. Our model allows for "sanity checks" on the coefficients R_{lin}, R_{quad}, and L (for instance, we expect L to be negative). This type of interpretability is important for high-stakes applications like cardiovascular flow modeling. Third, the proposed hybrid physics-ML formulation leverages a physics-based structure (instead of attempting to predict pressure differences directly from the bifurcation geometry and flow rate) which reduces the amount of data needed to train our models without overfitting. Since generating training data is expensive in this application, this is a major advantage.

The study of the combined dataset illustrates the generalizability and modest data demands of the RRI model structure. In combining the pulmonary and brachiocephalic datasets we roughly doubled the parameter ranges for all eight input features. To handle an input space of such increased size, one might expect that substantially more training data would be needed. However, we approximately doubled the amount of training data supplied to the ML model and achieved satisfactory accuracy. While additional data would likely have improved the performance of the combined model (especially at steady-state), this finding highlights the capability of the RRI model to handle a wide range of bifurcations using relatively little additional training data.

Finally, the structure of our model makes it straightforward to incorporate into existing ROM solvers. When a vasculature containing a junction is represented as a ROM, the ML model is evaluated once to predict the R_{quad}, R_{lin}, and L from the junction geometry. Since these coefficients are only functions of the geometry, they remain fixed throughout the ROM simulation while the solution variables of P, Q, and $\dot{Q}$ vary as the solver converges to a solution that satisfies the system of equations governing the flow, as in Fig. 3. Computationally, this is advantageous from both an implementation and efficiency perspective. Notably, the ML model only has to be evaluated once as a preprocessing stage, not at every solver iteration. Furthermore, the derivative of the residual contribution from (5) with respect to the solution variables is computationally cheap to evaluate.

5. Limitations and future work

While this work takes significant steps towards improving ROMs by accounting for the pressure differences over vascular bifurcations, there are challenges to be overcome before the proposed model can be widely deployed. These include expansion of the model to cover a wider range of junctions and incorporation of the model into ROM solvers.

To be most useful, our model should be able to predict the ΔP-Q relationship over any vascular junction it encounters. In this work, we analyzed two idealized, limited cohorts of bifurcations that do not represent the full range of native vascular bifurcations. To broaden our model's applicability, future work should consider larger datasets with parameter ranges that reflect the full ranges observed in the native anatomy. Moreover, future studies should consider datasets that capture observed variability in realistic bifurcation geometries, including geometric complexities such as curvature, stenoses, and aneurysms. Furthermore, a junction pressure loss model may need to handle junction geometries more complex than simple bifurcations. For instance, a vessel may split into more than two daughter branches or blood may flow from multiple inlets into one or more outlets (e.g., in backflow). There are several approaches to handle this; for instance, future work could generalize our NN regressor, which predicts the coefficients that govern the ΔP-Q relationship between the inlet and outlet of a junction to a graph neural network (GNN) [91]. Thanks to its flexible structure, a GNN will be capable of handling junctions with any number of inlets and outlets. Having seen in this work that NNs are capable of capturing the behavior of flow in a bifurcation; we predict that a GNN will be able to predict the ΔP-Q relationship on a junction with an arbitrary number of inlets and outlets with similar accuracy. Finally, while the simplicity of the RRI model form provides interpretability and generalizability, it could limit accuracy in some cases. Some complex flows may not be adequately captured by the RRI form, for instance non-Newtonian flow through capillary bifurcations. In such cases, additional terms may need to be added to the model, or a different model forms may be considered. It should be noted however that the bifurcations considered in this work, which represent a wide range of the geometries and flow conditions observed in the body, were well-modeled by the RRI form. Furthermore, in the context of reduced order modeling, the benefits of a simpler model form could outweigh associated decrease in accuracy, which may be negligible compared to the errors inherently introduced by the simplifications in reduced-order models [31].

A second challenge will be the incorporation of our RRI model into current ROMs. In most cases, this will require only minimal changes to the code. For instance, in SimVascular's 0D solver, the only necessary change will be to replace the equations enforcing equal pressure between junction outlets and inlets with equations enforcing the pressure difference predicted by our model. The greater difficulty will be the standardization of the definition of a junction. This is a general challenge encountered when translating 3D vasculatures into reduced-order systems because there is no straightforward definition of the boundary between a junction and a vessel. In this work, we defined the vessel-bifurcation boundaries heuristically, based on where the flow exhibits fully developed Poiseuille behavior, free of splitting effects caused by the bifurcation. This system worked for our study because we had a standardized geometry-generation method and an understanding of the flow-splitting behavior, but it would not work for generic use where there is no a priori general knowledge of the flow. The inaccuracies introduced by uncertainty in junction definition may be somewhat mitigated by the inclusion of the junction length in the feature set supplied to the ML model, but complicate the problem and may present difficulties when the RRI model encounters alternatively defined junctions. These challenges should be addressed in future studies that demonstrate improved performance of ROM solvers with the RRI model added.

6. Conclusions

We presented an RRI model that represents the pressure difference between a bifurcation inlet and outlet as the voltage difference over a serially connected linear resistor, quadratic resistor, and inductor.

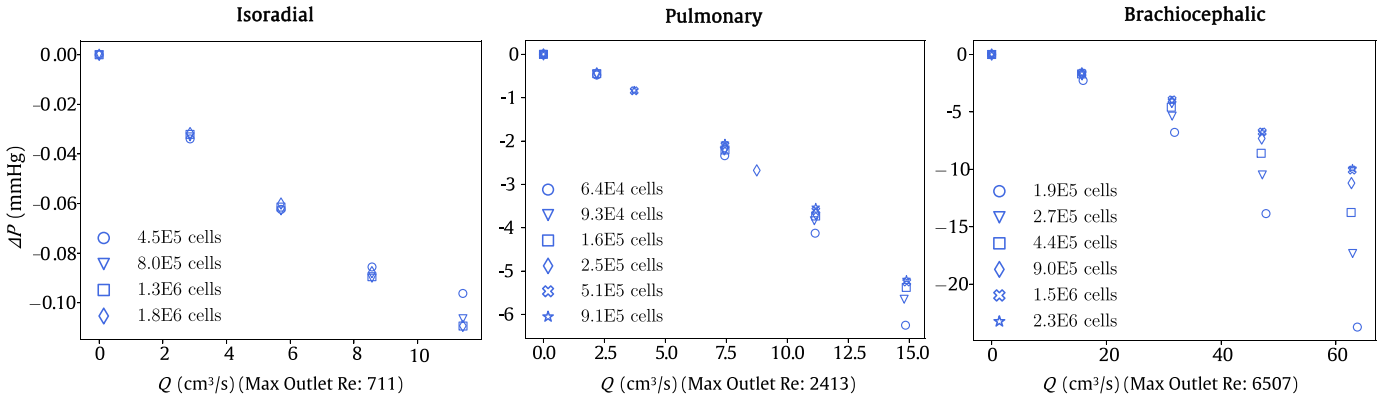

Fig. 8. Mesh refinement on isoradial bifurcation, pulmonary and brachiocephalic bifurcations.

The model uses ML to predict the resistances and inductance from the bifurcation geometry. To generate data on which to train and validate our model, we developed an automated pipeline to generate and simulate flow through bifurcations. We studied three types of bifurcations representing the nominal isoradial bifurcation considered in [74], the brachiocephalic bifurcation, and pulmonary bifurcations.

The RRI model performed well on various geometry types in both steady and transient flows. In the analysis of steady flows, we saw that the RRI model outperformed both the constant pressure assumption and the Unified0D+ model on all three bifurcation types considered. The study of transient flows again demonstrated the RRI model's strong performance and highlighted the importance of the flow time-derivative "inductor" term, which is absent from most other bifurcation pressure loss models. Comparison of different candidate machine learning techniques for fitting the RRI model coefficients indicated that the neural network produced the most accurate results most consistently. We observed that fitting the RRI coefficients using only transient data led to a slight improvement in accuracy for transient flows, compared to using both steady and transient data, but we noted that this approach compromises the physical interpretability of the RRI model. Finally, we found that the RRI model performed surprisingly well on a dataset with much larger feature ranges and comparatively little additional training data, indicating its ability to generalize well.

The RRI model presents a viable method to account for bifurcation pressure differences in cardiovascular ROMs, thus overcoming a major limitation of their accuracy. More accurate ROMs will add significant value to the cardiovascular flow modeling community, both in support of 3D CFD simulations as surrogate models for many-query applications (e.g., uncertainty quantification and boundary condition tuning) and in their own right as stand-alone models for real-time applications. In addition to contributing to more accessible and accurate patient-specific cardiovascular flow analysis, this work highlights opportunities for synergy between 3D CFD, physics-based reduced-order modeling, and data-driven techniques in medical research.

CRediT authorship contribution statement

Natalia L. Rubio: Writing – review & editing, Writing – original draft, Visualization, Validation, Software, Methodology, Investigation, Conceptualization. **Luca Pegolotti:** Writing – review & editing, Supervision, Software, Methodology, Investigation, Conceptualization. **Martin R. Pfaller:** Writing – review & editing, Supervision, Software, Methodology, Investigation, Conceptualization. **Eric F. Darve:** Writing – review & editing, Supervision, Methodology, Investigation, Conceptualization. **Alison L. Marsden:** Writing – review & editing, Supervision, Software, Resources, Project administration, Methodology, Investigation, Funding acquisition, Conceptualization.

Declaration of competing interest

None Declared.

Acknowledgments

This work was funded by the Stanford Graduate Fellowship and the National Science Foundation Graduate Research Fellowship Program. Additional support was provided by NIH Grants R01LM01312003, R01EB02936204, R01HL16751601, and K99HL161313, and the Stanford Maternal and Child Health Research Institute. The authors also thank Dr. Karthik Menon and Zachary Sexton for their helpful insight and discussions.

Appendix A. Mesh convergence

Fig. 8 shows convergence studies of steady flow simulations for decreasing mesh size for each bifurcation type. These studies guided our choice of mesh size.

Appendix B. Parameter ranges

The geometric parameters characterizing the isoradial and brachiocephalic cohorts of bifurcations were uniformly sampled from the ranges shown in Table 5. The isoradial ranges were found by varying the nominal parameters used in [74] ±20%. The pulmonary and brachiocephalic ranges were the 40th to 60th percentiles of the range of parameter values observed in distal pulmonary and brachiocephalic bifurcations, respectively, found in the VMR [75]. *Note:* for the pulmonary and brachiocephalic cohorts, the outlet radii were not sampled, but were computed as the product of the inlet radius and outlet–inlet radius ratio, both of which were sampled.

Appendix C. Hyperparameter optimization

The hyperparameters for the candidate ML models, shown in Table 6, were chosen using Ray Tune [90]. The objective minimized in the Ray Tune optimization was the error on the test set of steady flows through brachiocephalic junctions, and the resulting hyperparameters were used for all 3 cohorts for steady and transient models. *Note:* for the NN trained on the isoradial cohort, a hidden layer size of 70 was found (manually) to be optimal.

Table 5
Ranges for parameters in isoradial, pulmonary, and brachiocephalic bifurcation datasets.

Parameter:	Inlet radius (cm)	Outlet radius (cm)	Outlet angle (°)	Inlet velocity (cm/s)
Isoradial	0.44–0.66	0.44–0.66	36–54	49–74
Pulmonary	0.28–0.37	0.16–0.27	13–19	95–140
Brachiocephalic	0.46–0.59	0.28–0.43	16–24	127–180

Table 6
Values found using Ray Tune for hyperparameter optimization of candidate ML models.

Parameter	Value
K nearest neighbors	
Number of neighbors	7
Decision Tree	
Maximum depth	4
Minimum samples per leaf	8
Support vector regression	
C (L2 regularization parameter)	1.4
ϵ (no-penalty margin)	0.029
Gaussian process regression	
α (regularization parameter)	0.0020
Radial basis function kernel length scale	1.6
Neural network	
Hidden layer size	48
Number of hidden layers	2
Learning rate	0.018
Learning rate decay	0.031
Batch size	24

References

[1] E.L. Schwarz, L. Pegolotti, M.R. Pfaller, A.L. Marsden, Beyond CFD: Emerging methodologies for predictive simulation in cardiovascular health and disease, Biophys. Rev. (ISSN: 26884089) 4 (1) (2023) http://dx.doi.org/10.1063/5.0109400.

[2] C.A. Figueroa, C.A. Taylor, A.L. Marsden, Blood flow, in: Encyclopedia of Computational Mechanics Second Edition, Wiley, 2017, pp. 1–31, http://dx.doi.org/10.1002/9781119176817.ecm2068, URL https://onlinelibrary.wiley.com/doi/10.1002/9781119176817.ecm2068.

[3] H. Kamada, M. Nakamura, H. Ota, S. Higuchi, K. Takase, Blood flow analysis with computational fluid dynamics and 4D-flow MRI for vascular diseases, (ISSN: 18764738) 2022.

[4] P.D. Morris, A. Narracott, H. Von Tengg-Kobligk, D. Alejandro, S. Soto, S. Hsiao, A. Lungu, P. Evans, N.W. Bressloff, P.V. Lawford, R. Hose, J.P. Gunn, Computational fluid dynamics modelling in cardiovascular medicine, Heart 102 (2016) 18–28, http://dx.doi.org/10.1136/heartjnl, URL http://heart.bmj.com/.

[5] B.K. Lee, Computational fluid dynamics in cardiovascular disease, (ISSN: 17385555) 2011.

[6] D. Sengupta, A.M. Kahn, J.C. Burns, S. Sankaran, S.C. Shadden, A.L. Marsden, Image-based modeling of hemodynamics in coronary artery aneurysms caused by Kawasaki disease, Biomech. Model. Mechanobiol. (ISSN: 16177959) 11 (6) (2012) 915–932, http://dx.doi.org/10.1007/s10237-011-0361-8.

[7] D. Sengupta, A.M. Kahn, E. Kung, M. Esmaily Moghadam, O. Shirinsky, G.A. Lyskina, J.C. Burns, A.L. Marsden, Thrombotic risk stratification using computational modeling in patients with coronary artery aneurysms following Kawasaki disease, Biomech. Model. Mechanobiol. (ISSN: 16177940) 13 (6) (2014) 1261–1276, http://dx.doi.org/10.1007/s10237-014-0570-z.

[8] K. Menon, J. Seo, A.M. Kahn, J.C. Burns, A.L. Marsden, The risk of myocardial ischemia in patients with Kawasaki disease: Insights from patient-specific simulations of coronary hemodynamics, 2022, http://dx.doi.org/10.1101/2022.09.08.22279654, MedRxiv.

[9] N. Grande Gutierrez, M. Mathew, B.W. McCrindle, J.S. Tran, A.M. Kahn, J.C. Burns, A.L. Marsden, Hemodynamic variables in aneurysms are associated with thrombotic risk in children with Kawasaki disease, Int. J. Cardiol. (ISSN: 18741754) 281 (2019) 15–21, http://dx.doi.org/10.1016/j.ijcard.2019.01.092.

[10] F. Migliavacca, G. Dubini, E.L. Bove, M.R. De Leval, Computational fluid dynamics simulations in realistic 3-D geometries of the total cavopulmonary anastomosis: The influence of the inferior caval anastomosis, J. Biomech. Eng. (ISSN: 01480731) 125 (6) (2003) 805–813, http://dx.doi.org/10.1115/1.1632523.

[11] E.L. Bove, M.R. De Leval, F. Migliavacca, G. Guadagni, G. Dubini, Computational fluid dynamics in the evaluation of hemodynamic performance of cavopulmonary connections after the norwood procedure for hypoplastic left heart syndrome, J. Thorac. Cardiovasc. Surg. (ISSN: 00225223) 126 (4) (2003) 1040–1047, http://dx.doi.org/10.1016/S0022-5223(03)00698-6.

[12] E. Kung, A. Baretta, C. Baker, G. Arbia, G. Biglino, C. Corsini, S. Schievano, I.E. Vignon-Clementel, G. Dubini, G. Pennati, A. Taylor, A. Dorfman, A.M. Hlavacek, A.L. Marsden, T.Y. Hsia, F. Migliavacca, Predictive modeling of the virtual hemi-fontan operation for second stage single ventricle palliation: Two patient-specific cases, J. Biomech. (ISSN: 00219290) 46 (2) (2013) 423–429, http://dx.doi.org/10.1016/j.jbiomech.2012.10.023.

[13] M.L. Dong, I.S. Lan, W. Yang, M. Rabinovitch, J.A. Feinstein, A.L. Marsden, Computational simulation-derived hemodynamic and biomechanical properties of the pulmonary arterial tree early in the course of ventricular septal defects, Biomech. Model. Mechanobiol. (ISSN: 16177940) 20 (6) (2021) 2471–2489, http://dx.doi.org/10.1007/s10237-021-01519-4.

[14] K.S. Hunter, P.F. Lee, C.J. Lanning, D.D. Ivy, K.S. Kirby, L.R. Claussen, K.C. Chan, R. Shandas, Pulmonary vascular input impedance is a combined measure of pulmonary vascular resistance and stiffness and predicts clinical outcomes better than pulmonary vascular resistance alone in pediatric patients with pulmonary hypertension, Am. Heart J. (ISSN: 00028703) 155 (1) (2008) 166–174, http://dx.doi.org/10.1016/j.ahj.2007.08.014.

[15] W. Yang, M. Dong, M. Rabinovitch, F.P. Chan, A.L. Marsden, J.A. Feinstein, Evolution of hemodynamic forces in the pulmonary tree with progressively worsening pulmonary arterial hypertension in pediatric patients, Biomech. Model. Mechanobiol. (ISSN: 16177940) 18 (3) (2019) 779–796, http://dx.doi.org/10.1007/s10237-018-01114-0.

[16] B.T. Tang, S.S. Pickard, F.P. Chan, P.S. Tsao, C.A. Taylor, J.A. Feinstein, Wall shear stress is decreased in the pulmonary arteries of patients with pulmonary arterial hypertension: An image-based, computational fluid dynamics study, Pulm. Circ. (ISSN: 20458940) 2 (4) (2012) 470–476, http://dx.doi.org/10.4103/2045-8932.105035.

[17] M.X.G. Valentim, F.S.F. Zinani, C.E. da Fonseca, D.P. Wermuth, Systematic review on the application of computational fluid dynamics as a tool for the design of coronary artery stents, (ISSN: 23148543) 2023.

[18] T.J. Gundert, A.L. Marsden, W. Yang, J.F. Ladisa, Optimization of cardiovascular stent design using computational fluid dynamics, J. Biomech. Eng. (ISSN: 01480731) 134 (1) (2012) http://dx.doi.org/10.1115/1.4005542.

[19] A.O. Frank, P.W. Walsh, J.E. Moore, Computational fluid dynamics and stent design, Artif. Organs. (ISSN: 0160564X) 26 (7) (2002) 614–621, http://dx.doi.org/10.1046/j.1525-1594.2002.07084.x.

[20] S. Sankaran, M.E. Moghadam, A.M. Kahn, E.E. Tseng, J.M. Guccione, A.L. Marsden, Patient-specific multiscale modeling of blood flow for coronary artery bypass graft surgery, Ann. Biomed. Eng. (ISSN: 00906964) 40 (10) (2012) 2228–2242, http://dx.doi.org/10.1007/s10439-012-0579-3.

[21] J. Seo, A.B. Ramachandra, J. Boyd, A.L. Marsden, A.M. Kahn, Computational evaluation of venous graft geometries in coronary artery bypass surgery, Semin. Thorac. Cardiovasc. Surg. (ISSN: 15329488) 34 (2) (2022) 521–532, http://dx.doi.org/10.1053/j.semtcvs.2021.03.007.

[22] A.B. Ramachandra, A.M. Kahn, A.L. Marsden, Patient-specific simulations reveal significant differences in mechanical stimuli in venous and arterial coronary grafts, J. Cardiovasc. Transl. Res. (ISSN: 19375395) 9 (4) (2016) 279–290, http://dx.doi.org/10.1007/s12265-016-9706-0.

[23] W. Yang, J.A. Feinstein, A.L. Marsden, Constrained optimization of an idealized Y-shaped baffle for the fontan surgery at rest and exercise, Comput. Methods Appl. Mech. Engrg. (ISSN: 00457825) 199 (33–36) (2010) 2135–2149, http://dx.doi.org/10.1016/j.cma.2010.03.012.

[24] W. Yang, T.A. Conover, R.S. Figliola, G.A. Giridharan, A.L. Marsden, M.D. Rodefeld, Passive performance evaluation and validation of a viscous impeller pump for subpulmonary fontan circulatory support, Sci. Rep. 13 (1) (2023) 12668.

[25] K.H. Fraser, M.E. Taskin, B.P. Griffith, Z.J. Wu, The use of computational fluid dynamics in the development of ventricular assist devices, (ISSN: 13504533) 2011.

[26] D. Bluestein, Utilizing computational fluid dynamics in cardiovascular engineering and medicine—What you need to know. Its translation to the clinic/bedside, (ISSN: 15251594) 2017.

[27] J. Engelke, C. Karmonik, F. Rengier, S. Partovi, A.F. Popov, A. Osswald, R. Arif, B. Schmack, P. Raake, A.R. Simon, A. Doesch, A. Weymann, J. Lotz, M. Karck, A. Ruhparwar, Competing flow between partial circulatory support and native cardiac output: A clinical computational fluid dynamics study, ASAIO J. (ISSN: 1538943X) 64 (5) (2018) 636–642, http://dx.doi.org/10.1097/MAT.0000000000000701.

[28] S.S. Hossain, S.F. Hossainy, Y. Bazilevs, V.M. Calo, T.J. Hughes, Mathematical modeling of coupled drug and drug-encapsulated nanoparticle transport in patient-specific coronary artery walls, Comput. Mech. (ISSN: 01787675) 49 (2) (2012) 213–242, http://dx.doi.org/10.1007/s00466-011-0633-2.

[29] G. Bao, Y. Bazilevs, J.H. Chung, P. Decuzzi, H.D. Espinosa, M. Ferrari, H. Gao, S.S. Hossain, T.J. Hughes, R.D. Kamm, W.K. Liu, A. Marsden, B. Schrefler, Usnctam perspectives on mechanics in medicine, (ISSN: 17425662) 2014.

[30] S.S. Meschi, A. Farghadan, A. Arzani, Flow topology and targeted drug delivery in cardiovascular disease, J. Biomech. (ISSN: 18732380) 119, 42021, http://dx.doi.org/10.1016/j.jbiomech.2021.110307.

[31] M.R. Pfaller, J. Pham, N.M. Wilson, D.W. Parker, A.L. Marsden, On the periodicity of cardiovascular fluid dynamics simulations, Ann. Biomed. Eng. (ISSN: 15739686) 49 (12) (2021) 3574–3592, http://dx.doi.org/10.1007/s10439-021-02796-x.

[32] P.J. Nair, M.R. Pfaller, S.A. Dual, D.B. Mcelhinney, D.B. Ennis, A.L. Marsden, Non-invasive estimation of pressure drop across aortic coarctations: validation of 0D and 3D computational models with in vivo measurements, 2023, http://dx.doi.org/10.1101/2023.09.05.23295066, medRxiv.

[33] H.J. Kim, I.E. Vignon-Clementel, J.S. Coogan, C.A. Figueroa, K.E. Jansen, C.A. Taylor, Patient-specific modeling of blood flow and pressure in human coronary arteries, Ann. Biomed. Eng. (ISSN: 00906964) 38 (10) (2010) 3195–3209, http://dx.doi.org/10.1007/s10439-010-0083-6.

[34] N. Grande Gutiérrez, T. Sinno, S.L. Diamond, A 1D–3D hybrid model of patient-specific coronary hemodynamics, Cardiovasc. Eng. Technol. (ISSN: 18694098) 13 (2) (2022) 331–342, http://dx.doi.org/10.1007/s13239-021-00580-5.

[35] A.L. Brown, M. Salvador, L. Shi, M.R. Pfaller, Z. Hu, K.E. Harold, T. Hsiai, V. Vedula, A.L. Marsden, A modular framework for implicit 3D-0d coupling in cardiac mechanics, 2023, arXiv URL http://arxiv.org/abs/2310.13780.

[36] M.S. Olufsen, Structured tree outflow condition for blood flow in larger systemic arteries, Am. Physiol. Soc. J. 276 (1) (1999) 257–268.

[37] J. Seo, D.E. Schiavazzi, A.M. Kahn, A.L. Marsden, The effects of clinically-derived parametric data uncertainty in patient-specific coronary simulations with deformable walls, Int. J. Numer. Methods Biomed. Eng. (ISSN: 20407947) 36 (8) (2020) http://dx.doi.org/10.1002/cnm.3351.

[38] J. Seo, C. Fleeter, A.M. Kahn, A.L. Marsden, D.E. Schiavazzi, Multi-fidelity estimators for coronary circulation models under clinically-informed data uncertainty, Int. J. Uncertain. Quantif. 10 (5) (2020) 449–466.

[39] J.S. Tran, D.E. Schiavazzi, A.B. Ramachandra, A.M. Kahn, A.L. Marsden, Automated tuning for parameter identification and uncertainty quantification in multi-scale coronary simulations, Comput. & Fluids (ISSN: 00457930) 142 (2017) 128–138, http://dx.doi.org/10.1016/j.compfluid.2016.05.015.

[40] L.O. Müller, E.F. Toro, A global multiscale mathematical model for the human circulation with emphasis on the venous system, Int. J. Numer. Methods Biomed. Eng. (ISSN: 20407947) 30 (7) (2014) 681–725, http://dx.doi.org/10.1002/cnm.2622.

[41] H. Zhang, N. Fujiwara, M. Kobayashi, S. Yamada, F. Liang, S. Takagi, M. Oshima, Development of a numerical method for patient-specific cerebral circulation using 1D–0D simulation of the entire cardiovascular system with SPECT data, Ann. Biomed. Eng. (ISSN: 15739686) 44 (8) (2016) 2351–2363, http://dx.doi.org/10.1007/s10439-015-1544-8.

[42] J. Pham, S. Wyetzner, M.R. Pfaller, D.W. Parker, D.L. James, A.L. Marsden, svMorph: Interactive geometry-editing tools for virtual patient-specific vascular anatomies, J. Biomech. Eng. (ISSN: 15288951) 145 (3) (2023) http://dx.doi.org/10.1115/1.4056055.

[43] T.J.R. Hughes, J. Lubliner, On the one-dimensional theory of blood flow in the larger vessels, Math. Biosci. 18 (1–2) (1973) 161–170.

[44] N. Stergiopulos, D.F. Young, T.R. Rowe, Computer simulation of arterial flow with applications to arterial and aortic stenosis A A0 A, J. Biomech. 25 (12) (1992) 1477–1488.

[45] N. Westerhof, P. Sipkema, G.A.V. Huis, Coronary pressure-flow relations and the vascular waterfall, Cardiovasc. Res. (ISSN: 0008-6363) 17 (3) (1983) 162–169, http://dx.doi.org/10.1093/cvr/17.3.162.

[46] Y. Shi, P. Lawford, R. Hose, Review of Zero-D and 1-D models of blood flow in the cardiovascular system, (ISSN: 1475925X) 2011.

[47] J. Peiró, A. Veneziani, Reduced models of the cardiovascular system, in: Cardiovascular Mathematics, Springer Milan, Milano, 2009, pp. 347–394, http://dx.doi.org/10.1007/978-88-470-1152-6, URL http://link.springer.com/10.1007/978-88-470-1152-6_10.

[48] M.R. Pfaller, J. Pham, A. Verma, L. Pegolotti, N.M. Wilson, D.W. Parker, W. Yang, A.L. Marsden, Automated generation of 0D and 1D reduced-order models of patient-specific blood flow, Int. J. Numer. Methods Biomed. Eng. (ISSN: 20407947) 38 (10) (2022) http://dx.doi.org/10.1002/cnm.3639.

[49] M. Mirramezani, S.L. Diamond, H.I. Litt, S.C. Shadden, Reduced order models for transstenotic pressure drop in the coronary arteries, J. Biomech. Eng. (ISSN: 15288951) 141 (3) (2019) http://dx.doi.org/10.1115/1.4042184.

[50] L. Formaggia, A. Quarteroni, A. Veneziani, Cardiovascular Mathematics: : Modeling and Simulation of the Circulatory System, Springer Milano, 2010.

[51] A.R. Ghigo, P.Y. Lagrée, J.M. Fullana, A time-dependent non-Newtonian extension of a 1D blood flow model, J. Non-Newton. Fluid Mech. (ISSN: 03770257) 253 (2018) 36–49, http://dx.doi.org/10.1016/j.jnnfm.2018.01.004.

[52] S. Čanić, E.H. Kim, Mathematical analysis of the quasilinear effects in a hyperbolic model blood flow through compliant axi-symmetric vessels, Math. Methods Appl. Sci. (ISSN: 01704214) 26 (14) (2003) 1161–1186, http://dx.doi.org/10.1002/mma.407.

[53] M.S. Olufsen, 5. Modeling flow and pressure in the systemic arteries, in: In Applied Mathematical Models in Human Physiology, Society for Industrial and Applied Mathematics, 2004, pp. 91–136, http://dx.doi.org/10.1137/1.9780898718287.ch5.

[54] J. Wan, B. Steele, S.A. Spicer, S. Strohband, G.R. Feijóo, T.J. Hughes, C.A. Taylor, A one-dimensional finite element method for simulation-based medical planning for cardiovascular disease, Comput. Methods Biomech. Biomed. Eng. (ISSN: 10255842) 5 (3) (2002) 195–206, http://dx.doi.org/10.1080/10255840290010670.

[55] X. Wang, J.M. Fullana, P.Y. Lagrée, Verification and comparison of four numerical schemes for a 1D viscoelastic blood flow model, Comput. Methods Biomech. Biomed. Eng. (ISSN: 14768259) 18 (15) (2015) 1704–1725, http://dx.doi.org/10.1080/10255842.2014.948428.

[56] X.F. Wang, S. Nishi, M. Matsukawa, A. Ghigo, P.Y. Lagrée, J.M. Fullana, Fluid friction and wall viscosity of the 1D blood flow model, J. Biomech. (ISSN: 18732380) 49 (4) (2016) 565–571, http://dx.doi.org/10.1016/j.jbiomech.2016.01.010.

[57] A.M. Taylor-LaPole, M.J. Colebank, J.D. Weigand, M.S. Olufsen, C. Puelz, A computational study of aortic reconstruction in single ventricle patients, Biomech. Model. Mechanobiol. (ISSN: 16177940) 22 (1) (2023) 357–377, http://dx.doi.org/10.1007/s10237-022-01650-w.

[58] P. Reymond, F. Merenda, F. Perren, D. Rü, N. Stergiopulos, Validation of a one-dimensional model of the systemic arterial tree, Am. J. Physiol. Heart Circ. Physiol. 297 (2009) 208–222, http://dx.doi.org/10.1152/ajpheart.00037.2009.-A, URL http://www.ajpheart.orgH208.

[59] J.P. Mynard, J.J. Smolich, Novel wave power analysis linking pressure-flow waves, wave potential, and the forward and backward components of hydraulic power, Am. J. Physiol. Heart Circ. Physiol. 310 (2016) 1026–1038, http://dx.doi.org/10.1152/ajpheart.00954.2015.-Wave, URL www.ajpheart.org.

[60] J.M. Fullana, S. Zaleski, A branched one-dimensional model of vessel networks, J. Fluid Mech. (ISSN: 14697645) 621 (2009) 183–204, http://dx.doi.org/10.1017/S0022112008004771.

[61] S.J. Sherwin, L. Formaggia, J. Peiró, V. Franke, Computational modelling of 1D blood flow with variable mechanical properties and its application to the simulation of wave propagation in the human arterial system, Internat. J. Numer. Methods Fluids (ISSN: 02712091) 43 (6–7) (2003) 673–700, http://dx.doi.org/10.1002/fld.543.

[62] J. Lee, A. Cookson, I. Roy, E. Kerfoot, L. Asner, G. Vigueras, T. Sochi, S. Deparis, C. Michler, N.P. Smith, D.A. Nordsletten, Multiphysics computational modeling in cheart, SIAM J. Sci. Comput. (ISSN: 1064-8275) 38 (3) (2016) C150–C178, http://dx.doi.org/10.1137/15M1014097.

[63] J. Alastruey, S.R. Nagel, B.A. Nier, A.A. Hunt, P.D. Weinberg, J. Peiró, Modelling pulse wave propagation in the rabbit systemic circulation to assess the effects of altered nitric oxide synthesis, J. Biomech. (ISSN: 00219290) 42 (13) (2009) 2116–2123, http://dx.doi.org/10.1016/j.jbiomech.2009.05.028.

[64] J. Alastruey, K.H. Parker, S.J. Sherwin, Arterial pulse wave haemodynamics, in: S. Anderson (Ed.), 11th International Conference on Pressure Surges, Virtual PiE Led Ta BHR Group, 2012, pp. 401–443.

[65] J.P. Mynard, P. Nithiarasu, A 1D arterial blood flow model incorporating ventricular pressure, aortic vaive ana regional coronary flow using the locally conservative Galerkin (LCG) method, Commun. Numer. Methods Eng. (ISSN: 10698299) 24 (5) (2008) 367–417, http://dx.doi.org/10.1002/cnm.1117.

[66] P.J. Nair, M.R. Pfaller, S.A. Dual, M. Loecher, D.B. Mcelhinney, D.B. Ennis, A.L. Marsden, Hemodynamics in patients with aortic coarctation: A comparison of in vivo 4D-flow MRI and FSI simulation, 2023, http://dx.doi.org/10.1101/2023.02.13.528355, bioRxiv.

[67] O. San, A.E. Staples, An improved model for reduced-order physiological fluid flows, J. Mech. Med. Biol. (ISSN: 02195194) 12 (3) (2012) http://dx.doi.org/10.1142/S0219519411004666.

[68] C. Chnafa, K. Valen-Sendstad, O. Brina, V.M. Pereira, D.A. Steinman, Improved reduced-order modelling of cerebrovascular flow distribution by accounting for arterial bifurcation pressure drops, J. Biomech. (ISSN: 18732380) 51 (2017) 83–88, http://dx.doi.org/10.1016/j.jbiomech.2016.12.004.

[69] B.N. Steele, J. Wan, J.P. Ku, T.J. Hughes, C.A. Taylor, In vivo validation of a one-dimensional finite-element method for predicting blood flow in cardiovascular bypass grafts, IEEE Trans. Biomed. Eng. (ISSN: 00189294) 50 (6) (2003) 649–656, http://dx.doi.org/10.1109/TBME.2003.812201.

[70] W. Huberts, A.S. Bode, W. Kroon, R.N. Planken, J.H. Tordoir, F.N. van de Vosse, E.M. Bosboom, A pulse wave propagation model to support decision-making in vascular access planning in the clinic, Med. Eng. Phys. (ISSN: 13504533) 34 (2) (2012) 233–248, http://dx.doi.org/10.1016/j.medengphy.2011.07.015.

[71] D.J. Wood, L. Srinivasa Reddy, J.E. Funk, Modeling pipe networks dominated by junctions, J. Hydraul. Eng. 119 (8) (1993) 949–958.

[72] A. Gardel, Les pertes de charge dans les ecoulements au travers de branchements en Te: Stabilite des chambres d'equilibre: Influence de la partie de l'amenagement situee al'aval de la chambre d'equilibre sur les petites oscillations avec reglage automatique: Perte de charge dans un etranglement conique, Technical report, Communications du Laboratoire d'Hydraulique de l'Ecole Polytechnique Federale de Lausanne, 1971.

[73] M.D. Bassett, R.J. Pearson, N.P. Fleming, D.E. Winterbone, A multi-pipe junction model for one-dimensional gas-dynamic simulations, J. Engines 112 (2003) 565–583, URL https://about.jstor.org/terms.

[74] J.P. Mynard, K. Valen-Sendstad, A unified method for estimating pressure losses at vascular junctions, Int. J. Numer. Methods Biomed. Eng. (ISSN: 20407947) 31 (7) (2015) 1–23, http://dx.doi.org/10.1002/cnm.2717.

[75] N.M. Wilson, A.K. Ortiz, A.B. Johnson, The vascular model repository: A public resource of medical imaging data and blood flow simulation results, J. Med. Dev. (ISSN: 1932-6181) 7 (4) (2013) http://dx.doi.org/10.1115/1.4025983.

[76] M. Mirramezani, S.C. Shadden, A distributed lumped parameter model of blood flow, Ann. Biomed. Eng. (ISSN: 15739686) 48 (12) (2020) 2870–2886, http://dx.doi.org/10.1007/s10439-020-02545-6.

[77] R. Pewowaruk, L. Lamers, A. Roldán-Alzate, Accelerated estimation of pulmonary artery stenosis pressure gradients with distributed lumped parameter modeling vs. 3D CFD with instantaneous adaptive mesh refinement: Experimental validation in swine, Ann. Biomed. Eng. (ISSN: 0090-6964) 49 (9) (2021) 2365–2376, http://dx.doi.org/10.1007/s10439-021-02780-5.

[78] P.J. Blanco, C.A. Bulant, L.O. Müller, G.D. Talou, C.G. Bezerra, P.L. Lemos, R.A. Feijóo, Comparison of 1D and 3D models for the estimation of fractional flow reserve, Sci. Rep. (ISSN: 20452322) 8 (1) (2018) http://dx.doi.org/10.1038/s41598-018-35344-0.

[79] U.N.A. Qohar, A. Zanna Munthe-Kaas, J.M. Nordbotten, E.A. Hanson, A nonlinear multi-scale model for blood circulation in a realistic vascular system, R. Soc. Open Sci. 8 (12) (2021) http://dx.doi.org/10.1098/rsos.201949.

[80] M.R. Pfaller, L. Pegolotti, J. Pham, N.L. Rubio, A.L. Marsden, Reduced order modeling, in: T.C. Gasser, S. Avril, J.A. Elefteraides (Eds.), Biomechanics of the Aorta, Chapter 20, 1 ed., Elsevier, 2024.

[81] K.G. Lyras, J. Lee, An improved reduced-order model for pressure drop across arterial stenoses, PLoS One (ISSN: 19326203) 16 (10 October) (2021) http://dx.doi.org/10.1371/journal.pone.0258047.

[82] L. Itu, P. Sharma, K. Ralovich, V. Mihalef, R. Ionasec, A. Everett, R. Ringel, A. Kamen, D. Comaniciu, Non-invasive hemodynamic assessment of aortic coarctation: Validation with in vivo measurements, Ann. Biomed. Eng. (ISSN: 00906964) 41 (4) (2013) 669–681, http://dx.doi.org/10.1007/s10439-012-0715-0.

[83] A. Updegrove, N.M. Wilson, J. Merkow, H. Lan, A.L. Marsden, S.C. Shadden, SimVascular: An open source pipeline for cardiovascular simulation, Ann. Biomed. Eng. (ISSN: 0090-6964) 45 (3) (2017) 525–541, http://dx.doi.org/10.1007/s10439-016-1762-8.

[84] O. Kramer, K-Nearest Neighbors, Vol. 51, Intelligent Systems Reference Library, Springer, Berlin, Heidelberg, 2013, pp. 13–23, http://dx.doi.org/10.1007/978-3-642-38652-7.

[85] L. Breiman, J.H. Friedman, R.A. Olshen, C.J. Stone, Classification and Regression Trees, Routledge, New York, ISBN: 9781315139470, 2017, http://dx.doi.org/10.1201/9781315139470.

[86] M. Awad, R. Khanna, Support vector regression, in: Efficient Learning Machines, Apress, Berkeley, CA, 2015, pp. 67–80, http://dx.doi.org/10.1007/978-1-4302-5990-9.

[87] C.E. Rasmussen, C.K.I. Williams, Gaussian Processes for Machine Learning, The MIT Press, ISBN: 9780262256834, 2005, http://dx.doi.org/10.7551/mitpress/3206.001.0001.

[88] C.C. Aggarwal, Neural Networks and Deep Learning, Springer International Publishing, Cham, ISBN: 978-3-031-29641-3, 2023, http://dx.doi.org/10.1007/978-3-031-29642-0.

[89] T. Hauck, Scikit-Learn Cookbook, Packt Publishing, 2014.

[90] R. Liaw, E. Liang, R. Nishihara, P. Moritz, J.E. Gonzalez, I. Stoica, Tune: A research platform for distributed model selection and training, 2018, arXiv.

[91] F. Scarselli, M. Gori, Ah Chung Tsoi, M. Hagenbuchner, G. Monfardini, The graph neural network model, IEEE Trans. Neural Netw. (ISSN: 1045-9227) 20 (1) (2009) 61–80, http://dx.doi.org/10.1109/TNN.2008.2005605.